



HAL
open science

Multiwavelength analysis of short GRB 201221D and its comparison with other high & low redshift short GRBs

Dimple Dimple, K. Misra, D.A. Kann, K.G. Arun, A. Ghosh, R. Gupta, L. Resmi, J.F. Agüí Fernández, C.C. Thöne, A. de Ugarte Postigo, et al.

► To cite this version:

Dimple Dimple, K. Misra, D.A. Kann, K.G. Arun, A. Ghosh, et al.. Multiwavelength analysis of short GRB 201221D and its comparison with other high & low redshift short GRBs. *Monthly Notices of the Royal Astronomical Society*, 2022, 516 (1), pp.1-12. 10.1093/mnras/stac2162 . hal-03832730

HAL Id: hal-03832730





<https://hal.science/hal-03832730>

Submitted on 22 Apr 2024

HAL is a multi-disciplinary open access archive for the deposit and dissemination of scientific research documents, whether they are published or not. The documents may come from teaching and research institutions in France or abroad, or from public or private research centers.

L'archive ouverte pluridisciplinaire **HAL**, est destinée au dépôt et à la diffusion de documents scientifiques de niveau recherche, publiés ou non, émanant des établissements d'enseignement et de recherche français ou étrangers, des laboratoires publics ou privés.

Multiwavelength analysis of short GRB 201221D and its comparison with other high & low redshift short GRBs

Dimple ^{1,2}★, K. Misra ¹★, D. A. Kann,³ K. G. Arun,⁴ A. Ghosh ^{1,5}, R. Gupta,^{1,2} L. Resmi,⁶ J. F. Agüí Fernández ³, C. C. Thöne,³ A. de Ugarte Postigo,⁷ S. B. Pandey¹ and L. Yadav²

¹*Aryabhata Research Institute of Observational Sciences (ARIES), Manora Peak, Nainital 263002, India*

²*Department of Physics, Deen Dayal Upadhyaya Gorakhpur University, Gorakhpur 273009, India*

³*Instituto de Astrofísica de Andalucía, Glorieta de la Astronomía s/n, E-18008 Granada, Spain*

⁴*Chennai Mathematical Institute, Siruseri, 603103 Tamilnadu, India*

⁵*School of Studies in Physics and Astrophysics, Pandit Ravishankar Shukla University, Chattisgarh 492 010, India*

⁶*Indian Institute of Space Science and Technology, Trivandrum 695 547, India*

⁷*Artemis, Observatoire de la Côte D’Azur, Université Côte D’Azur, CNRS, Nice, F-06300, France*

Accepted 2022 July 27. Received 2022 July 25; in original form 2021 December 10

ABSTRACT

We present a detailed analysis of short GRB 201221D lying at redshift $z = 1.045$. We analyse the high-energy data of the burst and compare it with the sample of short gamma-ray bursts (SGRBs). The prompt emission characteristics are typical of those seen in the case of other SGRBs except for the peak energy (E_p), which lies at the softer end (generally observed in the case of long bursts). We estimate the host galaxy properties by utilizing the Python-based software *Prospector* to fit the spectral energy distribution of the host. The burst lies at a high redshift relative to the SGRB sample with a median redshift of $z = 0.47$. We compare the burst characteristics with other SGRBs with known redshifts along with GRB 200826A (SGRB originated from a collapsar). A careful examination of the characteristics of SGRBs at different redshifts reveals that some of the SGRBs lying at high redshifts have properties similar to long GRBs indicating they might have originated from collapsars. Further study of these GRBs can help to explore the broad picture of progenitor systems of SGRBs.

Key words: gamma-ray bursts: general – gamma-ray bursts: individual (GRB 201221D).

1 INTRODUCTION

The bi-modality in duration distribution of Gamma-Ray Bursts (GRBs) revealed two broad populations identified as short and long GRBs (based on T_{90} duration¹ with separation boundary at 2 s, Mazets et al. 1981; Kouveliotou et al. 1993). The two GRB populations are likely originating from two distinct progenitor systems, with different redshift distribution and located in diverse host galaxy environments (Nakar 2007; Berger 2014; Levan et al. 2016). The association of long GRBs with broad-lined supernovae of Type Ic and their occurrence in star-forming galaxies confirmed their association with collapsars (Woosley 1993; MacFadyen & Woosley 1999; Hjorth et al. 2003; Woosley & Bloom 2006; Li, Zhang & Lü 2016). On the other hand, a mix of young and old stellar population of host galaxies of SGRBs and the lack of associated supernova suggests that at least a fraction of SGRBs originate from compact object mergers (Berger 2009; Fong et al. 2013; Beniamini & Piran 2016). The discovery of gravitational wave signal GW170817 and its association with SGRB 170817A confirmed this hypothesis (Abbott et al. 2017; Goldstein et al. 2017; Valenti et al. 2017).

However, some of the long GRBs (like GRBs 060614 and 060505) have no evidence of supernova association despite long follow-up (Della Valle et al. 2006; Fynbo et al. 2006; Gal-Yam et al. 2006). Similarly, signatures of collapsars are seen in some of the SGRBs (for example, SGRBs 090426 and 200826A, Antonelli et al. 2009; Nicuesa Guelbenzu et al. 2011, 2012; Thöne et al. 2011; Ahumada et al. 2021; Rossi et al. 2021; Zhang et al. 2021). The absence of supernova signatures in long GRBs and the occurrence of SGRBs from collapsars challenge our current understanding of GRB population and their progenitor systems. Several attempts have been made in the past to devise new classification schemes based on different criteria other than T_{90} . Zhang (2006) divided the GRBs into Type I (compact star origin) and Type II (massive star origin) classes. Bromberg et al. (2013) classified the GRBs as collapsars and non-collapsars based on the non-collapsar probability. Later, Minaev & Pozanenko (2020) used the $E_{\gamma, \text{iso}} - E_{p, i}$ correlation to divide the GRBs in two classes. These works have allowed to develop a classification scheme beyond the traditional T_{90} distribution.

The distance measurement of the bursts can also provide essential information about their intrinsic energy budgets, the progenitor age distribution, and its relation to star-formation (Guetta & Piran 2005; Berger et al. 2007; Ghirlanda et al. 2009; D’Avanzo 2015). Therefore, the redshift distribution of GRBs serves as a clue to the progenitor systems. SGRBs are generally found at low redshifts (with a median redshift $\bar{z} = 0.47$) compared to long GRBs (with a median redshift

* E-mail: dimplepanchal96@gmail.com (DP); kuntal@aries.res.in (KM)

¹ T_{90} is the duration over which a particular instrument observes 5 per cent to 95 per cent of the total counts.

$\bar{z} = 1.68$; see Section 4 for details). The redshift distribution of SGRBs can be explained through their formation channel. The time taken by compact objects to merge (through energy/angular momentum loss by GW radiation) is quite long (Belczynski et al. 2006; Beniamini, Hotokezaka & Piran 2016). Therefore, if SGRBs originate from compact object mergers, they are more likely to lie at lower redshifts. However, a fraction of SGRBs are found to be located at high redshifts (Ugarte De Postigo et al. 2006; Berger et al. 2007).

It has also been observed that SGRBs at $z > 1$ have a high probability of being collapsars (Bromberg et al. 2013). It is also interesting to note that both the SGRBs 200826A ($z = 0.7481$; Rossi et al. 2021) and 090426 ($z = 2.609$; Antonelli et al. 2009), which have been found to originate from the death of massive stars, lie at the higher end of the redshift distribution of SGRBs. GRB 201221D is located at the higher end of the GRB redshift distribution ($z = 1.045$, Agüí Fernández et al. 2021), which gives rise to the question if the burst originates from a collapsar or a merger? In general, it is vital to investigate if the SGRBs lying at high redshifts have progenitor systems similar to the SGRBs lying at low redshifts? To address this question and the progenitor conundrum, we compare the properties of SGRBs in the context of the available redshift information.

The paper presents a detailed analysis of GRB 201221D and its comparison with other low and high redshift SGRBs. The data reduction procedure and analysis are described in Section 2. The results obtained are discussed in Section 3, including the properties of the host galaxy. In addition, we compare the SGRBs with known redshift to identify the similarities and differences between high and low redshift SGRB samples in Section 4. A brief summary of this work is presented in Section 5. We quote all the uncertainties at 1σ throughout this paper (unless otherwise mentioned). We used the Hubble parameter $H_0 = 70 \text{ km sec}^{-1} \text{ Mpc}^{-1}$, and the density parameters $\Omega_\Lambda = 0.73$ and $\Omega_m = 0.27$ in this paper. The measured redshift of $z = 1.045$ corresponds to a luminosity distance of 7109 Mpc.

2 DATA ACQUISITION AND ANALYSIS

Swift triggered on GRB 201221D on 2020 December 21, with the burst having a duration of 0.3 s (Page et al. 2020). The *Fermi* and *Konus-Wind* missions also detected the burst (Frederiks et al. 2020; Hamburg et al. 2020). Later, various ground-based telescopes started observations of the burst location to search its optical counterpart. Spectroscopic observations of the optical counterpart of GRB 201221D with the Gran Telescopio Canarias (GTC) provided the measurement of the redshift of $z = 1.045$ (Ugarte de Postigo et al. 2020). We also observed the burst location with the 3.6 m Devasthal Optical Telescope (DOT) and detected an extended source at the location of the burst (Dimple et al. 2020).

This section describes the data acquisition and analysis, using the data from different space- and ground-based instruments, in the prompt emission and afterglow phase.

2.1 *Swift*/BAT

GRB 201221D triggered the Burst Alert Telescope (BAT; Barthelmy et al. 2005) on-board the *Neil Gehrels Swift Observatory* (*Swift* hereafter) on 2020 December 21 at 23:06:34 UT. The best localization of the source was found to be at RA: 11 h 24 m 12 s and Dec: + 42 d 08 m 39 s (J2000) with an uncertainty radius of 3 arcmin (Page et al. 2020).

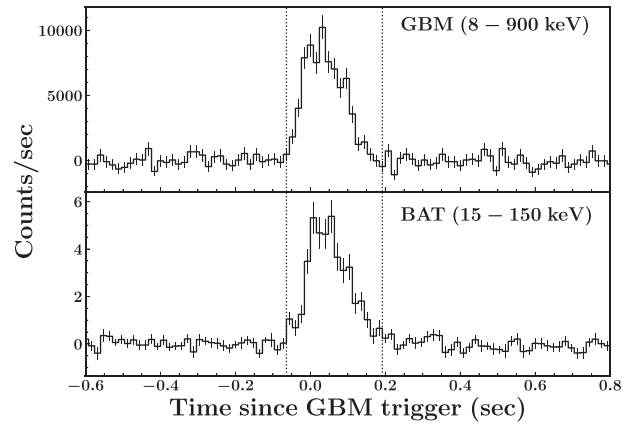


Figure 1. Light curves of GRB 201221D with a resolution of 64 ms in the energy ranges (8–900) keV and (15–150) keV using *Fermi*/GBM and *Swift*/BAT data, respectively. The dotted lines show the start and end times of the transient.

To extract the temporal and spectral features from the *Swift*/BAT data, we obtained the raw data from the *Swift* Archive Download Portal supported by the UK *Swift* Science Data Centre.² We utilized HEASOFT version-6.25 with the latest *Swift* calibration data files³ to reduce this data. The three primary tools, namely `batbinevt`, `bathotpix`, and `batmaskwtevt` were used to create the Detector Plane Image (DPI), to detect the hot pixels, and for mask-weighting, respectively. The mask-weighted light curve in the 15–150 keV energy range is extracted using `batbinevt`. The bottom panel of Fig. 1 shows the *Swift*/BAT light curve. The light curve consists of a single-peaked structure with a duration $T_{90} = 0.16 \pm 0.04$ s (Krimm et al. 2020; Page et al. 2020).

Furthermore, we obtained the time-averaged spectrum in a time interval starting from $T_0 - 0.064$ sec to $T_0 + 0.192$ sec following the method specified in the *Swift*/BAT software guide.⁴ The `pha` and response files obtained are used for joint spectral analysis along with *Fermi* data (see Section 2.3).

2.2 *Fermi*/GBM

The Gamma-Ray Burst Monitor (GBM, Meegan et al. 2009) on-board the *Fermi* spacecraft triggered and located GRB 201221D at 23:06:34.33 UT. Initially, the flight software classified the trigger as a particle event. Later, it was confirmed to be an SGRB with a T_{90} duration of about 0.14 s (50–300 keV). The burst location provided by *Fermi* was consistent with the *Swift*/BAT position (Hamburg et al. 2020). We used the time-tagged event (TTE) data of GBM obtained from the GBM trigger data archive⁵ for spectral and temporal analysis of the burst in the high-energy regime. We chose the detectors with low observing angles and high count rates. Three sodium iodide (NaI) detectors: n7, n8, and nb were selected by visually inspecting the count-rate light curves and source observing angles (n7 – 43°, n8 – 5°, nb – 57°). One of the bismuth germanate detectors (BGO1 – 61°), closer to the direction of burst, was also included in our analysis.

²https://www.swift.ac.uk/swift_portal/

³<https://heasarc.gsfc.nasa.gov/FTP/caldb/>

⁴https://swift.gsfc.nasa.gov/analysis/bat_swguide_v6.3.pdf

⁵<https://heasarc.gsfc.nasa.gov/FTP/fermi/data/gbm/triggers/>

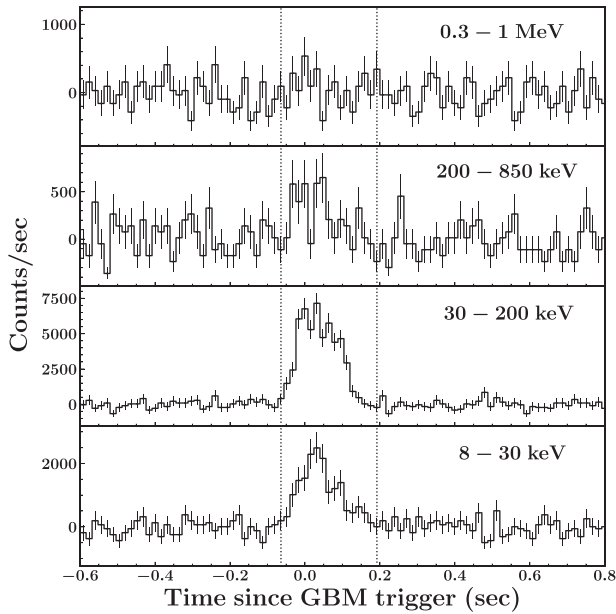


Figure 2. Prompt emission light curves of GRB 201221D in different energy channels of *Fermi*/GBM with a time resolution of 64 ms. The burst duration in higher energy channels is shorter than that in lower energy channels.

We used RMFIT⁶ (version 4.3.2) to visualize the light curves from the TTE files. From these light curves, we carefully selected the source and background. We fitted the background with various polynomial functions. The best-fitted background was subtracted from the source to produce light curves in different energy bins. The background-subtracted multichannel prompt emission γ -ray/hard X-ray light curves are shown in Fig. 2.

For spectral analysis, the background-fitted time-averaged spectrum for the time bin between $T_0 - 0.064$ to $T_0 + 0.192$ sec was obtained using the GTBURST software from the *Fermi Science Tools*. The pha files obtained are used for joint spectral analysis along with *Swift* data (see Section 2.3).

2.3 Joint *Swift* and *Fermi* spectral analysis

To investigate the emission mechanism of GRB 201221D, we performed a joint spectral analysis of *Fermi*/GBM and *Swift*/BAT data using threeML (3ML,⁷ Vianello et al. 2015) version 2.3.1. Joint spectral analysis was done utilizing the *Fermi*/GBM spectrum over the energy range of 8–900 keV (for NaI) and 200–30 000 keV (BGO) and the *Swift*/BAT data with energy range 15–150 keV. We removed the 33–37 keV energy channels to ignore the K-edge (33.17 keV) of the Na line from the spectral analysis of NaI data. We tried to fit the spectrum with a power-law function having an exponential cutoff (CPL model), Band function and Black Body along with Band function. Based on the Bayesian Information Criteria (BIC; Kass & Rafferty 1995), Akaike Information Criteria (AIC), and Log(likelihood) for each model, we found that the spectrum is best described with a CPL with power-law index of -0.20 ± 0.16 and cutoff energy $E_c = 51.14_{-6.7}^{+7.2}$ keV, which is re-parametrized to

Table 1. The best-fitting models and the spectral parameters obtained from time-resolved spectroscopy of GRB 201221D.

Time interval (s)	Model	α	E_p (keV)	Flux ($10^{-6} \text{ erg s}^{-1} \text{ cm}^{-2}$)
-0.044 – -0.005	CPL	$-0.34_{-0.54}^{+0.51}$	47_{-15}^{+22}	$2.6_{-2.1}^{+2.2}$
-0.005–0.112	CPL	$-0.37_{-0.19}^{+0.20}$	45_{-5}^{+6}	$3.8_{-2.4}^{+7.0}$
0.112–0.191	CPL	$-1.09_{-0.66}^{+0.67}$	18_{-5}^{+7}	$0.34_{-0.32}^{+1.2}$

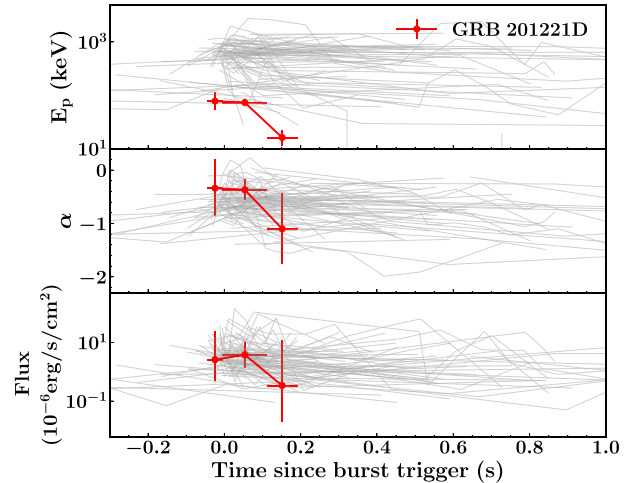


Figure 3. Evolution of spectral parameters for GRB 201221D and its comparison with the sample of SGRBs taken from Burgess et al. (2019). The photon index and flux values are typically comparable to the SGRB sample. However, the peak energy value of the burst is quite low in the last bin compared to the sample of SGRBs. All these parameters follow a hard-to-soft evolution.

$E_p = 110.4_{-13}^{+14}$ keV with a fluence of $(1.02 \pm 0.1) \times 10^{-6} \text{ erg cm}^{-2}$, consistent with the values reported by Hamburg et al. (2020).

2.3.1 Time-resolved spectroscopy

For time-resolved spectral analysis, we created the time bins from background-subtracted *Fermi*/GBM light curves by applying the bayesian blocks (Scargle et al. 2013) to the main emission interval ($T_0 - 0.064$ to $T_0 + 0.192$ s). We used the NaI-8 detector with the maximum count rate and obtained four Bayesian bins. However, we could use only three bins for spectral analysis as the first bin did not have sufficient counts to be modelled. We created the spectra for three bins and fitted them with various models (Band, Black Body, and CPL). We found that all of these spectra are well described with the CPL function. The best-fit model and the spectral parameters obtained from the time-resolved spectroscopy for GRB 201221D are listed in Table 1.

The evolution of spectral parameters is shown in Fig. 3. All the parameters (flux, α , and E_p) are seen to follow the same evolution pattern. The figure also shows a comparison of the evolution of parameters with an SGRB sample presented in Burgess et al. (2019). The values of different parameters in the case of GRB 201221D are typical, following a hard-to-soft evolution, as compared to the sample of SGRBs except for the cut-off energy, which lies at the lower end of the distribution.

⁶<https://fermi.gsfc.nasa.gov/ssc/data/analysis/rmfit/>

⁷<https://threeML.readthedocs.io/en/latest/>

Table 2. AB magnitudes of the afterglow/host of GRB 201221D. Magnitudes are not corrected for Galactic extinction.

Δt (days)	Filter	Magnitude (AB)	Telescope	Reference
0.069	r'	23.10 ± 0.30	NOT	Malesani & Knudstrup (2020)
0.115	r'	23.95 ± 0.20	GTC	Agüí Fernández et al. (2021)
0.400	J	21.8 ± 0.20	MMT	Rastinejad et al. (2020)
0.421	r'	~ 23.90	LMI	Dichiara et al. (2020)
0.421	i'	~ 23.70	LMI	Dichiara et al. (2020)
0.997	r'	23.62 ± 0.30	DOT	This Work
13.879	J	22.40 ± 0.17^h	LBT	Agüí Fernández et al. (2021)
13.895	K_s	22.15 ± 0.20^h	LBT	Agüí Fernández et al. (2021)
19.349	g'	23.80 ± 0.12^h	LBT	Agüí Fernández et al. (2021)
19.349	r'	23.83 ± 0.15^h	LBT	Agüí Fernández et al. (2021)
19.349	i'	23.44 ± 0.18^h	LBT	Agüí Fernández et al. (2021)
19.349	z'	23.11 ± 0.25^h	LBT	Agüí Fernández et al. (2021)
–	y	22.6 ± 0.20^h	Pan-STARRS	Kilpatrick, Malesani & Fong (2020)
165.75	R_C	$> 23.20^h$	DOT	This Work
175.66	R_C	$> 22.90^h$	HCT	This Work

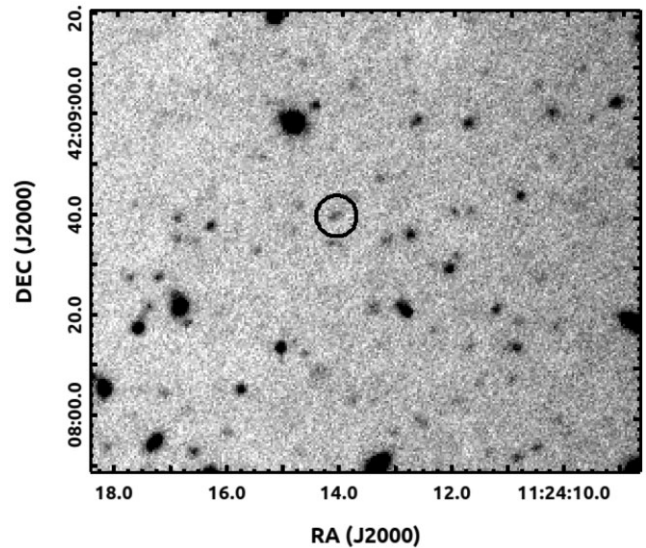
^h – Host magnitudes

2.4 *Swift*/XRT

The X-ray telescope (XRT; Burrows et al. 2005) on-board *Swift* started observing the field at 23:08:01.7 UT, 87.4 s after the BAT trigger. A new, faint, uncatalogued X-ray source was detected at RA: 11 h 24 m 14.19 s, Dec: + 42 d 08 m 35.5 s (J2000) with an uncertainty of $5''.7$ (radius, 90 per cent containment). Due to the faintness of the source, XRT observed it only in Photon Counting (PC) mode. The X-ray afterglow light curve, available at the *Swift* online repository⁸ provided by the University of Leicester (Evans et al. 2007, 2009), consists of only one data point (with a large error in time) followed by an upper limit. Further investigation of the X-ray afterglow could not be performed. However, in Section 4 we compare the X-ray light curves of SGRBs, including GRB 201221D.

2.5 Optical

The optical afterglow emission of GRB 201221D was discovered using the Nordic Optical Telescope (NOT) at ~ 1.67 h after the burst with $r' = 23.1 \pm 0.3$ mag (Malesani & Knudstrup 2020). Spectroscopic observations with the GTC/Optical System for Imaging and low Resolution Integrated Spectroscopy (OSIRIS) at ~ 2.76 hr after the burst showed evidence of absorption lines (Agüí Fernández et al. 2021), yielding a redshift $z = 1.045$. This is only the third spectrum of a SGRB afterglow (after GRB 130603B and GRB 160410A; Cucchiara et al. 2013; Ugarte de Postigo et al. 2014; Agüí Fernández et al. 2021) which displayed absorption-line features. The r' -band acquisition image from GTC/OSIRIS detected the afterglow with a magnitude of 23.95 ± 0.20 mag (Agüí Fernández et al. 2021). A source was also identified in the observations with the Large Monolithic Imager (LMI) on the 4.3 m Lowell Discovery Telescope in r' and i' bands at ~ 10.11 h (Dichiara et al. 2020). Further multiband observations of the host galaxy were also performed with the Multiple Mirror Telescope (MMT) and Large Binocular Telescope (LBT) (Agüí Fernández et al. 2021; Rastinejad et al. 2021; Rossi & CIBO Collaboration 2021). The optical/near-infrared (NIR) magnitudes of the afterglow/host available in the literature are listed in Table 2.

⁸<https://www.swift.ac.uk/>**Figure 4.** Optical image of GRB 201221D taken ~ 1 d after the burst using ADFOSC mounted on the 3.6 m DOT. An extended source can be clearly seen at the location of the burst.

2.5.1 Our observations

We observed the field of GRB 201221D using the $4K \times 4K$ ARIES Devasthal Faint Object Spectrograph and Camera (ADFOSC, Omar et al. 2019) mounted on 3.6 m DOT of ARIES Nainital. Four consecutive images of 15 min exposure time each were taken on 2022 December 22 (~ 1 d after the burst) in the r' band (Dimple et al. 2020). The pre-processing of the images, including bias subtraction, flat-field correction and cosmic ray removal, was performed using the *Astropy* and *CCDproc* modules in *Python*. The cleaned images were aligned using *astrowalign* and stacked using the *mediancombine* function of *CCDproc* to improve the signal-to-noise ratio. An extended source is visible at the position of the burst (Fig. 4). We performed PSF photometry on the stacked image using *DAOPHOT* and estimated the magnitude of the source to be $r' = 23.6 \pm 0.3$ mag (calibrated for the Pan-STARRS catalog). The late-time host galaxy observations were carried out on 2021 June 14 with

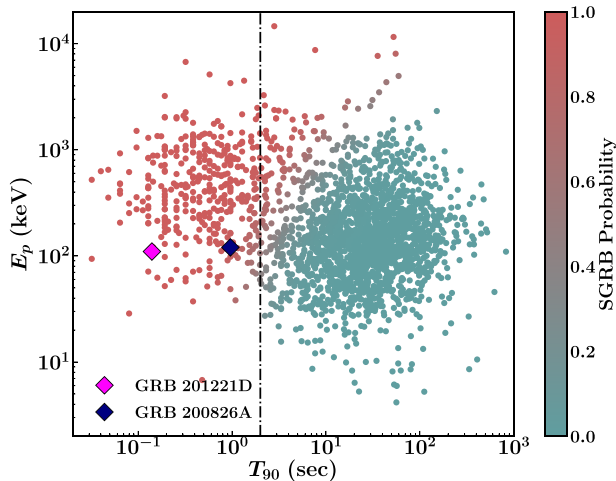


Figure 5. The $E_p - T_{90}$ distribution for GRBs taken from the *Fermi*/GBM catalogue. The magenta and blue diamonds indicate the location of GRB 201221D and GRB 200826A in the distribution. The vertical line shows the traditional separation between short and long GRB at 2 s. The colourbar on the right indicates the probability (estimated using BGMM) of GRBs being an SGRB.

the Hanle Faint Object Spectrograph and Camera (HFOSC) mounted on the 2.0 m Himalayan Chandra Telescope (HCT). Four images of exposure time 900 s each in the R_C band were recorded. No source was detected to a magnitude limit of 22.9 mag (AB) in the stacked image.

The field of GRB 201221D was also observed with the TIFR-ARIES Near-Infrared Spectrograph (TANSPEC), one of the main instruments of 3.6 m DOT (Sharma et al. 2022). We took ten consecutive frames in the R_C band with an exposure time of 500 sec each on 2021 June 4. The data pre-processing and photometry were performed in the same manner as described above. In the stacked image, we did not detect any source at the burst position to a magnitude limit of 23.2 mag (AB).

3 RESULTS

This section presents the results obtained from analysing the prompt emission of GRB 201221D and its host galaxy properties. Due to the unavailability of sufficient X-ray and optical data, we could not perform an afterglow analysis.

3.1 Spectral hardness and peak energy

The hardness ratio (HR) is calculated using the ratio of counts in two energy channels (the 10–50 keV and 50–300 keV energy bands) for the selected three NaI detectors. The HR is estimated to be 2.68 ± 0.83 , which is a typical value measured for SGRBs (3.61–5.64 with a mean value of 4.61; Ohno et al. 2008). We plot the $E_p - T_{90}$ distribution for all GRBs taken from the GBM catalog (Kienlin von et al. 2020). As described in Section 2.3, the value of E_p for GRB 201221D was calculated by a joint *Fermi*/GBM and *Swift*/BAT spectral fit. We fit the $E_p - T_{90}$ distribution with a Bayesian Gaussian Mixture Model (BGMM), which is a machine-learning clustering algorithm generally used for classification. We find a probability of 98 per cent for GRB 201221D to be a short burst. Fig. 5 shows the $E_p - T_{90}$ distribution along with the probability of a GRB being short. The probability of GRB 200826A being an SGRB is 74 per cent (Zhang

Table 3. Spectral lag of GRB 201221D in different energy channels with reference to the 8–30 keV band.

Energy channel (keV)	Spectral lag (ms)
30–50	$-19.2^{+3.82}_{-3.85}$
50–100	$-15.1^{+5.27}_{-5.50}$
100–150	$-19.0^{+3.41}_{-3.55}$
150–200	$-10.2^{+3.37}_{-3.40}$
200–250	$-13.0^{+5.40}_{-5.39}$
250–350	$+6.93^{+8.49}_{-7.86}$

et al. 2021). However, recent analysis indicates a collapsar origin for GRB 200826A (Ahumada et al. 2021; Rossi et al. 2021) unlike SGRBs, which are proposed to come from compact object mergers. Even though the probability of GRB 201221D belonging to the SGRB population is quite high, concerning the recent developments on GRB 200826A, we probe further to ascertain the classification of GRB 201221D.

3.2 Spectral lag

We calculate the spectral lag for GRB 201221D in different energy bands, selecting the range between 8–350 keV (a sufficient number of counts are not available beyond 350 keV), considering the 8–30 keV band as the reference channel. We estimate the temporal correlation of the two light curves using the cross-correlation function (CCF) as described in Bernardini et al. (2015). The maximum of the temporal correlation provides the delay between two light curves. To find the global maximum, we fit the correlation with an asymmetric Gaussian function using *emcee* (Foreman-Mackey et al. 2013). The spectral lag in different energy bands are quoted in Table 3 and the evolution is shown in the top panel of Fig. 6.

An anti-correlation has been found between the bolometric peak luminosity and the spectral lag of GRBs by Norris, Marani & Bonnell (2000), later confirmed by Norris (2002), Gehrels et al. (2006), Ukwatta et al. (2010). To put GRB 201221D in lag-luminosity correlation, we calculate the lag between the two energy channels (15–25 keV and 50–100 keV) of *Swift*/BAT to compare (the same energy channels used for the sample of GRBs defined in Ukwatta et al. 2010). The lag between the BAT energy channels is 7 ± 5 ms, close to zero within errors.

The burst does not lie within the 2σ region of the lag-luminosity correlation, as shown in the bottom panel of Fig. 6. On the other hand, the lag measured in GRB 200826A was 157 ms (Zhang et al. 2021), and it falls within the lag-luminosity correlation, which is generally true for long GRBs. It increases the ambiguity in the classification of GRB 200826A.

3.3 Non-collapsar probability

As discussed earlier, the origin of SGRBs belongs to old stellar populations and is supposed to lie at low redshifts (Leibler & Berger 2010; Fong et al. 2013), but GRB 201221D lies at a high redshift ($z = 1.045$) as compared to the median redshift of SGRBs. Therefore, to check if GRB 201221D originated from a collapsar or not, we estimate the non-collapsar probability (f_{nc}) using the functions defined in Bromberg et al. (2012), Bromberg et al. (2013):

$$f(T_{90}) = A_{NC} \frac{1}{T_{90}\sigma\sqrt{2\pi}} e^{-\frac{(\ln T_{90} - \mu)^2}{2\sigma^2}} \left(\frac{dN_{GRB}}{dT_{90}} \right)^{-1}, \quad (1)$$

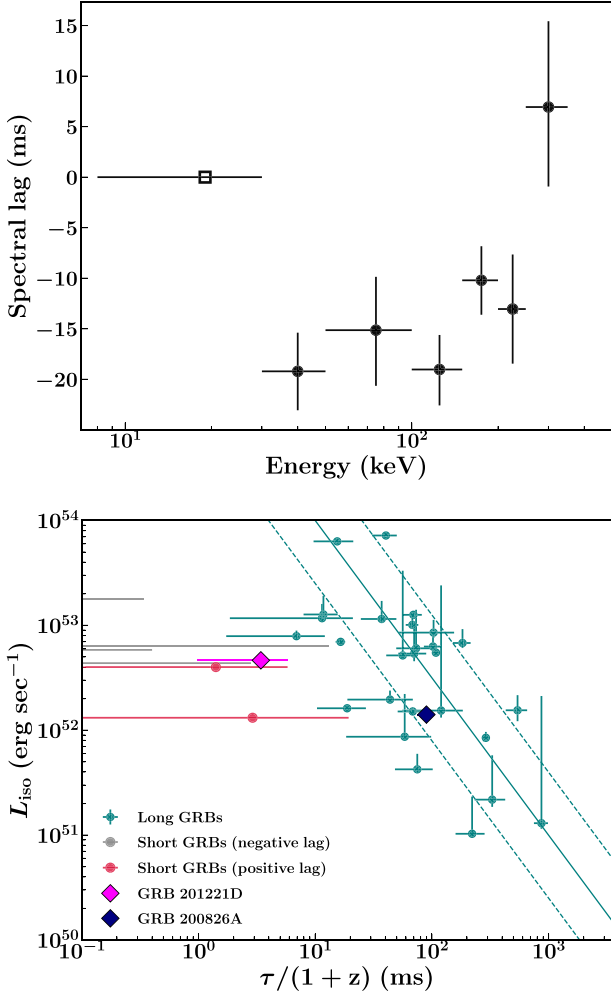


Figure 6. **Top:** The evolution of spectral lag for GRB 201221D in different energy channels using the *Fermi* data. The value of lag is close to zero, as expected in the case of SGRBs. **Bottom:** GRB 201221D and GRB 200826A in the lag-luminosity plane. GRB 201221D does not lie within the 2σ region (presented by dotted teal lines) of the lag-luminosity correlation. However, GRB 200826A follows this correlation, which is generally true for long GRBs.

where, dN_{GRB}/dT_{90} represents the non-collapsar distribution and is given by equation:

$$\frac{dN_{GRB}}{dT_{90}} = A_{NC} \frac{1}{T_{90}\sigma\sqrt{2\pi}} e^{-\frac{(\ln T_{90} - \mu)^2}{2\sigma^2}} + A_C \begin{cases} 1 & T_{90} \leq T_B \\ \left(\frac{T_{90}}{T_B}\right)^\alpha e^{-\beta(T_{90} - T_B)} & T_{90} > T_B. \end{cases} \quad (2)$$

The first and the second term correspond to non-collapsars and collapsars, respectively. T_B is the observed breakout time in the duration distribution. A_{NC} and A_C are the fit parameters and are taken from Bromberg et al. (2013) that they obtained by fitting the duration distributions to the collapsar distribution function.

Using T_{90} (*Fermi*/GBM) for GRB 201221D, we estimate the f_{nc} value of $0.86^{+0.09}_{-0.24}$. For comparison, we also calculate the f_{nc} value for GRB 200826A, which is $0.36^{+0.18}_{-0.16}$. The high probability of a non-collapsar origin for GRB 201221D shows that it very likely belongs to the non-collapsar progenitors.

Table 4. Host properties of GRB 201221D estimated from SED fitting using *Prospector*.

Host Properties	Priors	Values
$\log(M_*)$	9.0–11.0	$9.98^{+0.10}_{-0.09}$
$\log(Z/Z_\odot)$	-4.0–4.0	$-2.94^{+0.10}_{-0.08}$
$A_V(\text{mag})$	0–2.0	$0.26^{+0.26}_{-0.18}$
$t_{gal}(\text{Gyr})$	0–6.1	$1.79^{+0.56}_{-0.54}$
$\text{SFR}(M_\odot \text{yr}^{-1})$	–	2.92 ± 1.43

3.4 Host properties

The host galaxy of GRB 201221D was identified in the optical and NIR bands with LBT in late-time observations (Agüí Fernández et al. 2021). The host magnitudes are listed in Table 2. The available magnitudes are used to investigate the host galaxy properties using *Prospector* (Johnson et al. 2021). *Prospector* is a Python-based stellar population modelling code which uses Flexible Stellar Population synthesis (FSPS; Conroy, Gunn & White 2009; Conroy & Gunn 2010; Conroy 2013) to build the stellar population models (Leja et al. 2017; Johnson et al. 2021). It utilizes *Dynesty* (Speagle 2020), a nested sampling algorithm, to fit the photometric and spectroscopic data of a galaxy and provides the best-fit solution and posterior parameter distributions for the galaxy parameters. We used the best fit to determine the stellar mass (M), age of the galaxy (t_{gal}), star-formation history (SFH), dust extinction (A_V), and stellar metallicity (Z) using the methodology described in Johnson et al. (2021). We used the Milky Way extinction law and Chabrier initial mass function (Cardelli, Clayton & Mathis 1989; Chabrier 2003). We fixed the redshift to $z = 1.045$ (Agüí Fernández et al. 2021) and fitted for other parameters by setting the priors as listed in Table 4. The maximum value of the age of the galaxy is fixed to 6.148 Gyr, the age of the Universe at the redshift of the burst. The posterior distributions for the parameters produced using *Prospector* are shown in the corner plots in Fig. 7. The photometric data of the host overplotted with the model spectrum and photometry is shown in Fig. 8. We found the best-fitting values for the parameters as listed in Table 4 with log evidence value of 148 ± 36 . The values of the host parameters are consistent with the values derived in Agüí Fernández et al. (2021).

Further, we estimated the star formation rate (SFR) using the relation:

$$\text{SFR}(t) = M \times \left[\int_0^t t e^{-t/\tau} dt \right]^{-1} \times t e^{-t/\tau},$$

where, M is the total mass of the galaxy, t is the age of the galaxy and τ is star-formation time-scale. The value of SFR is given in Table 4. This relatively high value of SFR is consistent with the detection of O[II] emission from the host in the GTC spectrum.

4 ARE HIGH REDSHIFT SGRBS SIMILAR TO LOW REDSHIFT SGRBS?

Motivated by the fact that some of the SGRBs lying at a high redshift (e.g. GRBs 200826A and 090426A) have signatures of collapsars and earlier prediction by Berger et al. (2007) that there can be a new population of SGRBs at higher redshifts, we examine the similarity and differences between SGRBs at low and high redshifts.

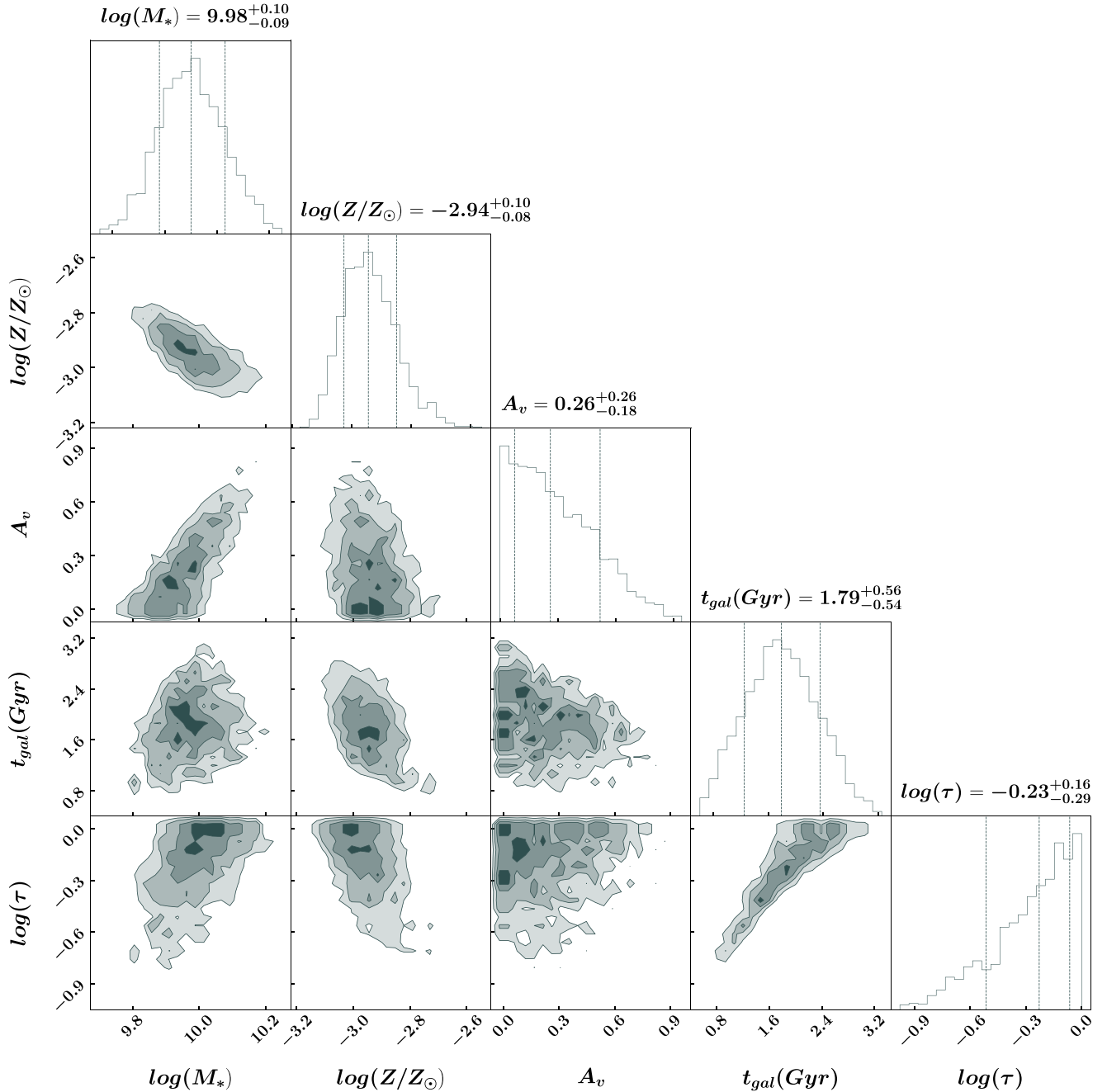


Figure 7. The posterior distributions for various host parameters obtained from *Prospector*.

We selected all the GRBs (both long and short available in Jochen Greiner’s compilation page⁹) up to 2021 October with known redshifts and calculated the redshift corrected T_{90} $T_{90,i}$. We selected all the GRBs with $T_{90,i} < 2$ s as the SGRBs in our sample. The full sample of 43 SGRBs is given in Table 5. We compared the redshift distribution of SGRBs with that of long GRBs. Fig. 9 shows the redshift distribution of GRBs. We estimated the median redshift value for SGRBs is $\bar{z} = 0.47$, which is lower than the estimated median redshift value of long GRBs ($\bar{z} = 1.68$). Considering the median redshift of SGRBs, we divide the sample of SGRBs into two

groups; Group 1-low redshift SGRBs with $z < 0.7$, and Group 2-high redshift SGRBs with $z \geq 0.7$.

In this section, we present the comparison of prompt (prompt emission correlations and f_{nc}) properties, afterglow, and the host properties of SGRBs lying at high and low redshifts.

4.1 Prompt emission properties

Prompt emission correlations have been used as tools to classify GRBs for a long time. In the Amati correlation plane, $E_{\gamma, iso} - E_{p,i}$ (peak energy in the source frame) plane, two classes of GRBs lie at different positions following different tracks (Amati et al. 2002; Amati 2006). Using the fluence value (1–1000 keV) and E_p values

⁹<https://www.mpe.mpg.de/~jcg/grbgen.html>

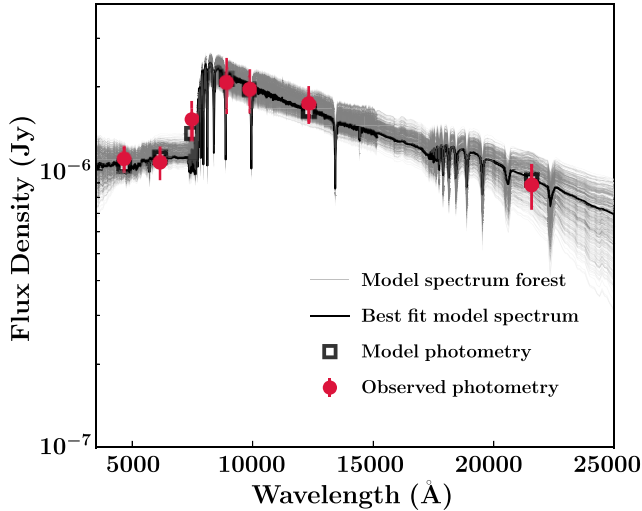


Figure 8. The host SED along with the 500 forest plots (light grey), which are randomly generated from the posterior distributions of the parameters obtained from *Prospector*. The black open squares and the thick black plot represents the best fit model photometry and best fit spectrum, respectively. The model photometry and spectrum are in agreement with the observed data.

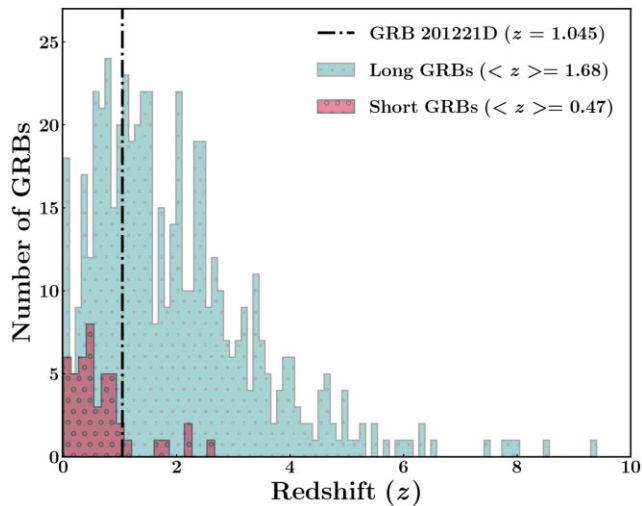


Figure 9. Redshift distribution of GRBs (both long and short) up to October 2021 (from Minaev & Pozanenko 2020 and Jochen Greiner’s compilation page). The SGRBs lie at the lower end of the redshift distribution with a median redshift of 0.47. Long GRBs are spread across the redshift distribution with a median of 1.68.

estimated in Section 2.3, we calculate the isotropic energy release and $E_{p,i}$ for GRB 201221D, $E_{\gamma, iso} = 2.762 \times 10^{51}$ erg, and $E_{p,i} = 226_{-35.8}^{+31.8}$.

We plot GRB 201221D in the Amati correlation plane along with SGRBs of Group 1 and Group 2 and long GRBs (Fig. 10) using the values of $E_{\gamma, iso}$, $E_{p,i}$ from Minaev & Pozanenko (2020). The dotted lines show the 2σ correlation regions. GRB 201221D lies in the overlapping 2σ regions of correlation of both short and long GRBs. In the figure, we also highlight the position of GRB 200826A, which follows the long GRB track. We also find that some SGRBs at $z > 0.7$ lie on the long GRB track and some in the overlapping 2σ correlation region of short and long GRBs.

In addition, we calculate $L_{\gamma, p, iso} = 4.64 \pm 0.84 \times 10^{52}$ and put GRB 201221D in the Yonetoku correlation plane ($L_{\gamma, p, iso} - E_{p,i}$) along with the sample available from the literature (Yonetoku et al. 2004; Nava et al. 2012). The bottom panel of Fig. 10 shows the location of the burst in the Yonetoku plane, GRB 201221D and GRB 200826A lie within the 3σ scatter of the sample of GRBs studied by Nava et al. (2012).

We also compare the non-collapsar probability (f_{nc}) of GRB 201221D and GRB 200826A with other SGRBs with a known redshift from the sample of Bromberg et al. (2013). Fig. 11 shows the f_{nc} for SGRBs lying at different redshifts. These results indicate that most of the SGRBs at high redshift ($z > 1$) have lower values of f_{nc} , which is in agreement with the results of Bromberg et al. (2013), indicating that these SGRBs might arise from progenitors other than compact object mergers.

4.2 Multiband SGRB afterglow light curves

We compare the optical (R_C/r') and X-ray (0.3–10 keV) afterglow light curves of Group 1 and Group 2 SGRBs, as defined earlier. We construct the optical light curves of SGRB afterglows using the data from Fong et al. (2015) up to 2015 and Rastinejad et al. (2021) for bursts beyond 2015. The magnitudes are converted to flux density after correcting for galactic extinction for each burst.

The X-ray light curves, in units of flux, in the energy range 0.3–10 keV, are taken from the *Swift* XRT repository.¹⁰ The flux light curves are converted to luminosity to compare Group 1 and Group 2 SGRBs. Fig. 12 shows the comparison between optical and X-ray light curves of Group 1 and Group 2 SGRBs. The optical light curves show a wide range in brightness for SGRBs at different redshifts. However, the X-ray luminosities for SGRBs at high redshifts (Group 1) are systematically higher than those of SGRBs at lower redshifts. The luminosity correlates with redshift due to the Malmquist bias. As a consequence, the faint bursts would not be detected at high-redshifts, where only luminous bursts can be detectable.

GRB 201221D does not have good coverage in both optical and X-ray bands. With the limited data GRB 201221D seems to lie at the lower end of the luminosity distribution in optical and X-ray bands.

4.3 Host properties

We compare the SFRs of the hosts of all SGRBs with known redshifts. The SFR values are taken from Berger (2014) and Dichiaro et al. (2021). In Fig. 13 we plot the SFR and stellar mass of all SGRB hosts along with GRB 201221D (this work) and GRB 200826A (Zhang et al. 2021) colour-coded with the redshift value. We notice that the hosts of SGRBs lying at higher redshifts have higher SFR values than those of SGRBs lying at lower redshifts. A recent study by Dichiaro et al. (2021) compared the SFRs of SGRB hosts at redshift $z > 1$ with those of long GRBs at redshift $1 < z < 2$. Their study indicated a significant overlap in SFR and stellar masses between short and long GRB hosts in this redshift range.

As SGRBs are supposed to originate from compact star mergers, they are believed to be associated with an old population of galaxies with low SFRs (Fong & Berger 2013; Berger 2014; Li et al. 2016). On the other hand, long GRBs, expected to originate from massive star collapsars, are generally found in star-forming galaxies with high SFRs. The overlap between the SFRs of long and SGRB hosts at redshift $z > 1$ indicates they might have the same type of progenitor

¹⁰https://www.swift.ac.uk/xrt_curves/

Table 5. Sample of SGRBs with known redshifts.

GRB	$T_{90,i}^{a,b}$ (s)	z^a	$E_{\gamma,iso}^a$ 10^{51} (erg)	Group 1 SGRBs			References ^c
				$E_{p,i}^a$ (keV)	f_{nc}	SFR (M_{\odot} year ⁻¹)	
GRB 050509B	0.04	0.2248	0.0024 ^{+0.004} _{-0.001}	100 ⁺⁷⁴⁸ ₋₉₈	0.87 ^{+0.04} _{-0.16}	<0.15	1, 2
GRB 050709	0.06	0.1606	0.027 ^{+0.011} _{-0.011}	96.3 ^{+20.9} _{-13.9}	0.92 ^{+0.02} _{-0.03}	0.15	1, 2
GRB 050724	2.4	0.2576	0.090 ^{+0.11} _{-0.02}	138 ⁺⁵⁰³ ₋₅₇	–	<0.1	2
GRB 051221A	0.14	0.5465	9.10 ^{+1.29} _{-1.12}	677 ⁺²⁰⁰ ₋₁₄₁	0.18 ^{+0.08} _{-0.11}	0.95	1, 2
GRB 060502B	0.12	0.287	0.433 ^{+0.053} _{-0.053}	438 ⁺⁵⁶¹ ₋₁₄₈	0.99 ^{+0.01} _{-0.16}	0.8	1, 2
GRB 061006	0.26	0.4377	3.82 ^{+0.73} _{-0.63}	909 ⁺²⁶⁰ ₋₁₉₁	–	0.24	2
GRB 061201	0.77	0.111	1.68 ^{+0.029} _{-0.029}	970 ⁺²⁹⁸ ₋₂₀₉	0.92 ^{+0.05} _{-0.08}	0.14	1, 2
GRB 070724A	0.27	0.457	0.016 ^{+0.003} _{-0.003}	119 ^{+7.30} _{-7.30}	0.37 ^{+0.26} _{-0.17}	2.5	1, 2
GRB 070809	0.44	0.2187	1.04 ^{+0.16} _{-0.16}	464 ⁺²²³ ₋₂₂₃	0.09 ^{+0.13} _{-0.05}	<0.1	1, 2
GRB 071227	1.30	0.384	0.591 ^{+0.025} _{-0.025}	875 ⁺⁷⁹⁰ ₋₂₈₇	0.71 ^{+0.15} _{-0.59}	0.6	1, 2
GRB 080123	0.27	0.495	3.20 ^{+6.59} _{-1.47}	2228 ⁺¹²⁷²³ ₋₁₃₀₈	–	–	
GRB 080905A	0.86	0.122	0.66 ^{+0.10} _{-0.10}	658 ⁺²⁹³ ₋₁₂₃	0.88 ^{+0.07} _{-0.11}	–	1
GRB 100206A	0.09	0.408	0.047 ^{+0.06} _{-0.06}	708 ^{+0.69} ₋₆₉	0.99 ^{+0.01} _{-0.01}	30	1, 2
GRB 100625A	0.13	0.452	0.75 ^{+0.03} _{-0.03}	706 ^{+0.116} ₋₁₁₆	0.97 ^{+0.02} _{-0.03}	0.3	1, 2
GRB 130603B [†]	0.16	0.356	1.96 ^{+0.10} _{-0.10}	823 ⁺⁸³ ₋₇₁	0.86 ^{+0.26} _{-0.26}	1.7	2
GRB 140903A [†]	0.22	0.351	0.044 ^{+0.003} _{-0.003}	60 ⁺²² ₋₂₂	0.78 ^{+0.08} _{-0.27}	1.0 ± 0.3	4
GRB 141212A [†]	0.19	0.596	0.068 ^{+0.011} _{-0.011}	151 ⁺¹⁴ ₋₁₄	0.78 ^{+0.07} _{-0.07}	–	
GRB 150101B [†]	0.02	0.093	0.0022 ^{+0.0003} _{-0.0003}	34 ⁺²³ ₋₂₃	0.86 ^{+0.08} _{-0.09}	≤0.4	5
GRB 150120A [†]	0.8	0.46	0.19 ^{+0.04} _{-0.04}	190 ⁺²²⁰ ₋₇₃	0.33 ^{+0.20} _{-0.10}	–	
GRB 150423A [†]	1.14	0.22	0.0075 ^{+0.001} _{-0.001}	146 ⁺⁴³ ₋₄₃	0.83 ^{+0.08} _{-0.10}	–	
GRB 160624A [†]	0.13	0.483	0.40 ^{+0.14} _{-0.15}	1247 ⁺⁵³¹ ₋₅₃₁	0.84 ^{+0.07} _{-0.07}	–	
GRB 160821B [†]	0.41	0.16	0.12 ^{+0.02} _{-0.02}	97.4 ⁺²² ₋₂₂	0.67 ^{+0.10} _{-0.10}	–	
GRB 170428A [†]	0.14	0.454	1.86 ^{+0.32} _{-0.98}	1428 ⁺³⁴⁶ ₋₃₁₃	0.85 ^{+0.09} _{-0.10}	–	
GRB 170817A [†]	0.50	0.00968	4.7e - 5 ^{+0.7e-5} _{-0.7e-5}	65.6 ^{+35.3} _{-14.1}	0.44 ^{+0.15} _{-0.13}	4e-3	6
Group 2 SGRBs							
GRB 050813	0.35	0.72	0.15 ^{+0.25} _{-0.08}	361 ⁺¹²²¹ ₋₂₂₄	0.57 ^{+0.36} _{-0.24}	–	1, 2
GRB 060121	0.28	4.6	180 ⁺¹² ₋₁₂	767 ⁺⁸⁴ ₋₆₇	0.17 ^{+0.14} _{-0.15}	–	1, 2
GRB 060801	0.33	1.131	180 ⁺¹² ₋₁₂	1321 ⁺¹³⁷⁹ ₋₄₃₉	0.95 ^{+0.03} _{-0.05}	6.1	1, 2
GRB 061217	0.19	0.827	4.23 ^{+0.72} _{-0.72}	731 ⁺⁸⁹⁵ ₋₂₈₇	0.98 ^{+0.01} _{-0.23}	2.5	1, 2
GRB 070429B	0.17	0.904	0.475 ^{+0.071} _{-0.071}	229 ⁺⁸⁵⁹ ₋₇₆	0.32 ^{+0.26} _{-0.15}	1.1	1, 2
GRB 070714B	0.65	0.923	6.4 ^{+1.1} _{-1.1}	1060 ⁺²⁸⁵ ₋₂₁₅	–	0.44	1, 2
GRB 070729	0.56	0.8	1.13 ^{+0.44} _{-0.44}	666 ⁺⁶⁷⁵ ₋₂₆₁	0.89 ^{+0.06} _{-0.57}	<0.15	1, 2
GRB 090426	0.33	2.609	8.4 ^{+1.9} _{-1.9}	1065 ⁺⁵⁹⁹ ₋₂₉₉	0.10 ^{+0.15} _{-0.06}	4.3 ^{+2.0} _{-2.0}	1, 3, 2
GRB 090510	0.51	0.903	54.6 ^{+2.1} _{-2.1}	7955 ⁺³⁴³ ₋₃₄₃	0.97 ^{+0.01} _{-0.29}	0.3	1, 2
GRB 100117A	0.27	0.915	7.8 ⁺¹ ₋₁	547 ⁺⁸⁴ ₋₈₄	0.97 ^{+0.01} _{-0.03}	<0.2	1, 2
GRB 101219A	0.30	0.718	6.51 ^{+0.36} _{-0.36}	1014 ⁺¹¹⁰ ₋₉₆	0.94 ^{+0.03} _{-0.06}	–	1, 2
GRB 111117A	0.18	2.211	8.9 ^{+3.4} _{-3.4}	1350 ⁺⁴⁵⁰ ₋₄₅₀	0.36 ^{+0.03} _{-0.05}	17.4 ^{+9.4} _{-6.6}	1, 3, 2
GRB 120804A	0.33	1.3	6.57 ^{+0.47} _{-0.47}	283 ⁺⁶² ₋₄₁	0.36 ^{+0.11} _{-0.19}	40 ⁺³³ ₋₂₈	3, 2
GRB 131004A [†]	0.90	0.71	0.69 ^{+0.03} _{-0.03}	202 ⁺⁵¹ ₋₅₁	0.24 ^{+0.07} _{-0.07}	–	
GRB 140622A [†]	0.07	0.959	0.10 ^{+0.02} _{-0.02}	86.2 ^{+15.7} _{-15.7}	0.89 ^{+0.27} _{-0.27}	–	
GRB 150424A [†]	0.14	1.0	52.3 ^{+1.9} _{-1.9}	1835 ⁺⁹⁹ ₋₉₄	0.59 ^{+0.19} _{-0.22}	–	
GRB 160410A	0.58	1.717	93 ⁺¹⁸ ₋₁₈	3853 ⁺¹⁴²³ ₋₉₇₃	0.59 ^{+0.19} _{-0.22}	–	3
GRB 200826A [†]	0.54	0.7486	7.09 ^{+0.28} _{-0.28}	210 ^{+6.8} _{-6.4}	0.36 ^{+0.18} _{-0.16}	>1.44	7
GRB 201221D*	0.06	1.045	2.76 ^{+0.21} _{-0.21}	226 ^{+31.8} _{-35.8}	0.86 ^{+0.09} _{-0.24}	2.92 ^{+1.43} _{-1.43}	This work

^a $T_{90,i}$, z , $E_{\gamma,iso}$, and $E_{p,i}$ values are taken from Minaev & Pozanenko (2020) except for GRB 200826A and GRB 201221D^b $T_{90,i} = T_{90}/(1+z)$ [†] Value of f_{nc} is estimated in this work^c References for f_{nc} and SFR; 1 – Bromberg et al. (2013), 2 – Berger (2014), 3 – Dichiara et al. (2021), 4 – Troja et al. (2016), 5 – Fong et al. (2016),

6 – Im et al. (2017), 7 – Zhang et al. (2021)

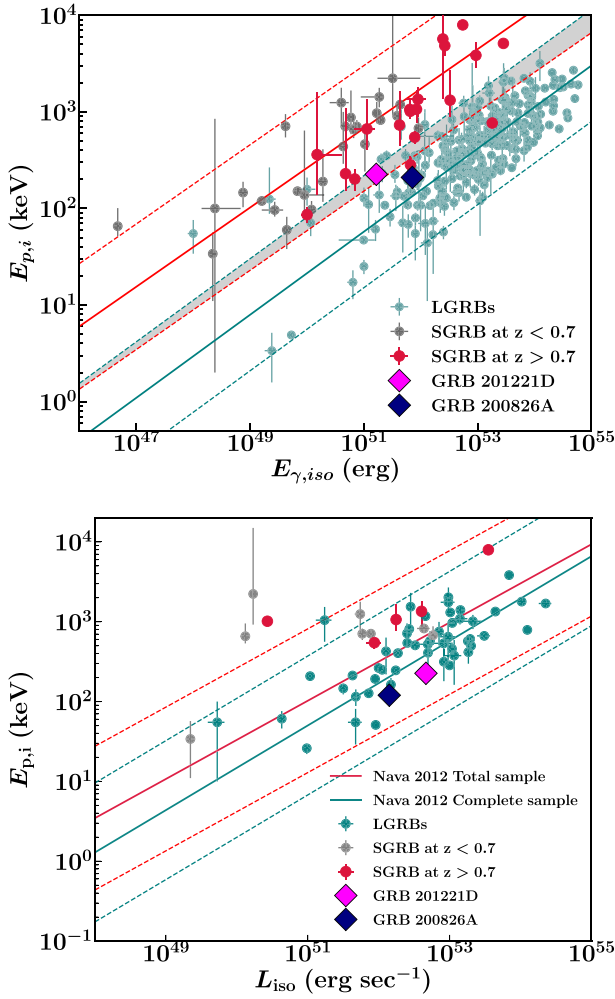


Figure 10. **Top:** Short and long GRBs in the Amati correlation plane. The SGRBs are divided into Group 1 (at $z < 0.7$, grey circles) and Group 2 ($z \geq 0.7$, crimson circles). The locations of GRB 201221D and GRB 200826A in the plane are shown with magenta and blue diamond symbols, respectively. GRB 200826A, along with some other SGRBs from Group 2 are seen to follow the track of long GRBs. However, GRB 201221D lies in the overlapping region of 2σ tracks of long and SGRBs. **Bottom:** Yonetoku correlation for Group 1, Group 2 SGRBs along with long GRBs. Both GRB 201221D and GRB 200826A follow the Yonetoku correlation and are situated well within the 2σ region of the correlation.

system. However, the galaxy properties also vary with redshift. In general, there is a steady decrease in the overall SFR of the Universe by a factor of 10 from $z=1$ to $z=0$ (Madau et al. 1996; Bauer et al. 2005).

5 SUMMARY

We have presented the analysis of GRB 201221D and its comparison with the SGRB sample. We determined the prompt emission parameters such as spectral hardness, lag, non-collapsar probability, and the host galaxy properties of the burst. We also performed the time-resolved spectroscopy of the prompt emission of GRB 201221D and compared the evolution with that of an SGRB sample from Burgess et al. (2019). The fit parameters, E_p (peak energy), α (spectral index), and flux show hard-to-soft evolution. The (α and flux) lie well within

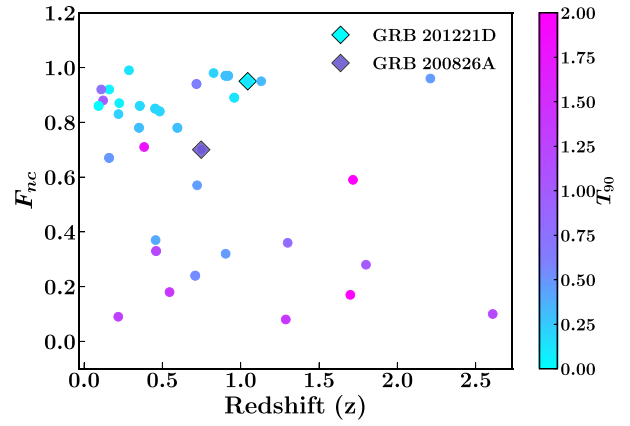


Figure 11. Non-collapsar probability of SGRBs along with their redshifts. The colourbar indicates the T_{90} values of SGRBs. The f_{nc} value is 0.4 for most of the SGRBs lying at $z > 1$, indicating that some of these SGRBs might have originated from collapsars.

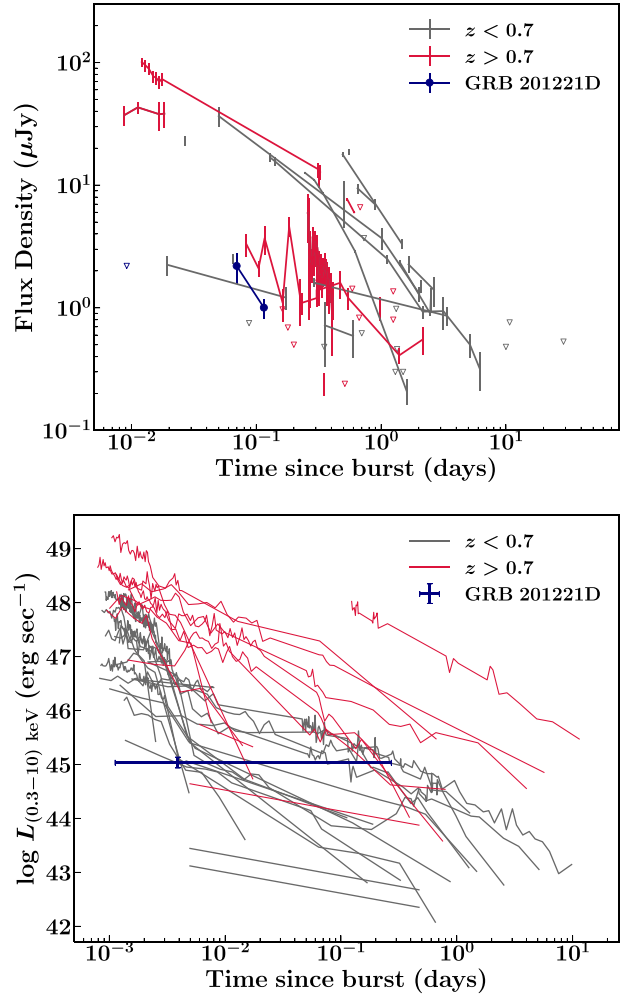


Figure 12. Optical and X-ray light curves of SGRBs. The sample of SGRBs is divided into Group 1 ($z < 0.7$) and Group 2 ($z \geq 0.7$) as indicated in the plot. The light curves of GRB 201221D are shown in blue colour.

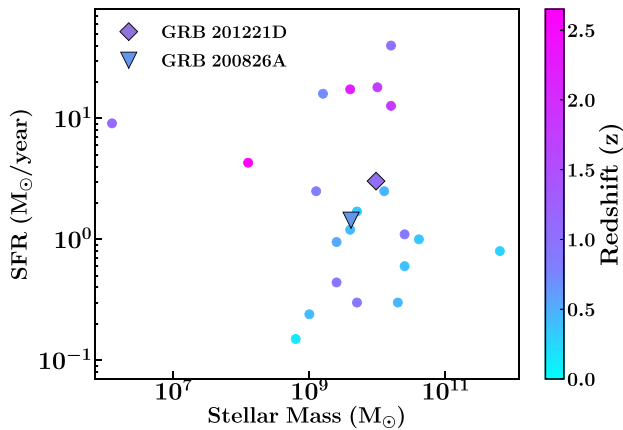


Figure 13. Star-formation rate and stellar mass of SGRB hosts colour-coded with the redshift value. The data are taken from Berger (2014), Dichiaro et al. (2021), Zhang et al. (2021), and this work. The SGRB hosts lying at higher redshifts have relatively larger SFR values than those for low-redshift SGRB hosts. GRB 201221D has an intermediate value compared to the sample of SGRBs studied here.

the usual range for the SGRB sample. The E_p value is softer than the SGRB sample and comparable to that of long GRBs.

As the T_{90} value depends on the sensitivity of an instrument and the background variations, it alone cannot decide the classification of a burst. It is essential to look for other properties that can be used for classification (Fenimore et al. 1995; Qin et al. 2000). We used different methods reported in the literature to confirm the class of GRB 201221D (Minaev & Pozanenko 2020; Dimple et al. 2022). We calculated the probability of GRB 201221D being an SGRB by fitting the $E_p - T_{90}$ distribution with BGMM. The probability of GRB 201221D is 98 per cent, indicating that GRB 201221D very likely belongs to SGRB class. Furthermore, we calculated the spectral lag in different energy bands, and the lag value is close to zero, as expected for SGRBs. We placed the burst in the Amati correlation plane. It lies in the overlapping region of short and long GRBs.

Furthermore, we compared the prompt (prompt emission correlation and f_{nc}), afterglow, and host properties of SGRBs lying at high and low redshifts to address the implication of redshift on the progenitor system of SGRBs. We found that:

(a) SGRBs with $z > 0.7$ are located close to the long GRB track in the Amati plane. Three SGRBs (including GRB 200826A) lie on the long GRB track. Some of these SGRBs, including GRB 201221D lie in the overlapping region of 2σ regions of long and SGRBs.

(b) The non-collapsar probabilities for some high redshift SGRBs have values < 0.5 , indicating these SGRBs might result from collapsars.

(c) The optical brightness of SGRBs covers a wide range at different redshifts. But the X-ray luminosities of SGRBs at high redshifts are systematically higher than those of SGRBs at lower redshifts. Also, a fraction of high redshift SGRB hosts has large SFR comparable to those of long GRB hosts. This difference can be explained through observational selection effects (e.g. Malmquist bias). The studies show that SGRBs lying at high redshifts have similarities to long GRBs, indicating they might have progenitor systems other than compact object mergers (e.g. GRB 200826A and GRB 090426), or there might exist subgroups within the SGRBs originating through different channels (Anand, Shahid & Resmi

2018; Yu et al. 2018; Gompertz, Levan & Tanvir 2020). The investigation of SGRBs lying in the overlapping region can provide a clearer picture of the progenitor systems of SGRBs.

Machine learning algorithms can play a crucial role to solve the classification conundrum (Jespersen et al. 2020; Dimple et al. 2022). In addition, late-time optical and NIR observations in the future can help to observe the bumps in the optical/NIR light curves in GRBs. It will lead to identifying the bumps as supernovae/kilonovae, which are uniquely associated with collapsars/compact binary mergers. However, it is difficult to detect the kilonova/supernova transients at higher redshifts due to the observational limitations and their faintness and fast evolution. The observations by future telescopes like Extremely Large Telescope (ELT), Thirty-Meter Telescope (TMT), and Giant Magellan Telescope (GMT) have the potential to detect kilonovae at redshift > 1 . In addition to optical observations, gravitational-wave observations have immense potential to shed light on this problem. However, only third-generation gravitational wave detectors such as Einstein Telescope and Cosmic Explorer (Sathyaprakash et al. 2012; Evans et al. 2021; Kalogera et al. 2021), expected to be operational in 2030 +, will have the sensitivity to observe binary neutron stars at redshifts around 1.

DATA AVAILABILITY

The optical data is already presented in the article, and other data sets are available in the public domain.

ACKNOWLEDGEMENTS

We thank the referee for the constructive comments which has improved the presentation of the article. KM, RG, and SBP acknowledge the BRICS grant DST/IMRCD/BRICS/PilotCall1/ProFCheap/2017(G) for the financial support. KGA is partially supported by the Swarnajayanti Fellowship Grant No.DST/SJF/PSA-01/2017-18, MATRICS grant MTR/2020/000177 of SERB, and a grant from the Infosys Foundation. This research is based on observations obtained from the 3.6 m DOT during observing cycle DOT-2020-C2, a National Facility run and managed by ARIES, an autonomous institute under the Department of Science and Technology (DST), Government of India. This research has used data obtained from the High Energy Astrophysics Science Archive Research Center (HEASARC) provided by NASA's Goddard Space Flight Center.

REFERENCES

- Abbott B. P. et al., 2017, *ApJ*, 848, L13
 Agüí Fernández J. F. et al., 2021, *MNRAS*, preprint (arXiv:2109.13838)
 Ahumada T. et al., 2021, *Nature Astron.*, 5, 917
 Amati L. et al., 2002, *A&A*, 390, 81
 Amati L., 2006, *MNRAS*, 372, 233
 Anand N., Shahid M., Resmi L., 2018, *MNRAS*, 481, 4332
 Antonelli L. A. et al., 2009, *A & A*, 507, L45
 Barthelmy S. D. et al., 2005, *Space Sci. Rev.*, 120, 143
 Bauer A. E., Drory N., Hill G. J., Feulner G., 2005, *ApJ*, 621, L89
 Belczynski K., Perna R., Bulik T., Kalogera V., Ivanova N., Lamb D. Q., 2006, *ApJ*, 648, 1110
 Beniamini P., Hotokezaka K., Piran T., 2016, *ApJ*, 829, L13
 Beniamini P., Piran T., 2016, *MNRAS*, 456, 4089
 Berger E. et al., 2007, *ApJ*, 664, 1000
 Berger E., 2009, *ApJ*, 690, 231
 Berger E., 2014, *ARA&A*, 52, 43
 Bernardini M. G. et al., 2015, *MNRAS*, 446, 1129

- Bromberg O., Nakar E., Piran T., Sari R., 2012, *ApJ*, 749, 110
- Bromberg O., Nakar E., Piran T., Sari R., 2013, *ApJ*, 764, 179
- Burgess J. M., Greiner J., Bégué D., Berlato F., 2019, *MNRAS*, 490, 927
- Burrows D. N. et al., 2005, *Space Sci. Rev.*, 120, 165
- Cardelli J. A., Clayton G. C., Mathis J. S., 1989, *ApJ*, 345, 245
- Chabrier G., 2003, *PASP*, 115, 763
- Conroy C., 2013, *ARA&A*, 51, 393
- Conroy C., Gunn J. E., 2010, *ApJ*, 712, 833–857
- Conroy C., Gunn J. E., White M., 2009, *ApJ*, 699, 486
- Cucchiara A. et al., 2013, *ApJ*, 777, 94
- D'Avanzo P., 2015, *JHEP*, 7, 73
- Della Valle M. et al., 2006, *Nature*, 444, 1050
- Dichiara S. et al., 2021, *Astrophys. J. Lett.*, 911, L28
- Dichiara S., Troja E., Cenko S. B., O'Connor B., Gatkine P., Durbak J. M., Kutyrev A., Veilleux S., 2020, *GCN Circ.*, 29128, 1
- Dimple et al., 2022, preprint ([arXiv:2202.01191](https://arxiv.org/abs/2202.01191))
- Dimple Panchal A., Gangopadhyay A., Ghosh A., Gupta R., Kumar A., Misra K., Pandey S. B., 2020, *GCN Circ.*, 29148, 1
- Evans M. et al., 2021, A Horizon Study for Cosmic Explorer: Science, Observatories, and Community, preprint ([arXiv:2109.09882](https://arxiv.org/abs/2109.09882))
- Evans P. A. et al., 2007, *A&A*, 469, 379
- Evans P. A. et al., 2009, *MNRAS*, 397, 1177
- Fenimore E. E., in 't Zand J. J. M., Norris J. P., Bonnell J. T., Nemiroff R. J., 1995, *ApJ*, 448, L101
- Fong W. et al., 2013, *ApJ*, 769, 56
- Fong W. et al., 2016, *ApJ*, 833, 151
- Fong W., Berger E., 2013, *ApJ*, 776, 18
- Fong W., Berger E., Margutti R., Zauderer B. A., 2015, *ApJ*, 815, 102
- Foreman-Mackey D., Hogg D. W., Lang D., Goodman J., 2013, *PASP*, 125, 306
- Frederiks D. et al., 2020, *GCN Circ.*, 29130, 1
- Fynbo J. P. U. et al., 2006, *Nature*, 444, 1047
- Gal-Yam A. et al., 2006, *Nature*, 444, 1053
- Gehrels N. et al., 2006, *Nature*, 444, 1044
- Ghirlanda G., Nava L., Ghisellini G., Celotti A., Firmani C., 2009, *A&A*, 496, 585
- Goldstein A. et al., 2017, *ApJ*, 848, L14
- Gompertz B. P., Levan A. J., Tanvir N. R., 2020, *ApJ*, 895, 58
- Guetta D., Piran T., 2005, *A&A*, 435, 421
- Hamburg R., Malacaria C., Meegan C., Fermi GBM Team, 2020, *GCN Circ.*, 29140, 1
- Hjorth J. et al., 2003, *Nature*, 423, 847
- Im M. et al., 2017, *ApJ*, 849, L16
- Jespersen C. K., Severin J. B., Steinhardt C. L., Vinther J., Fynbo J. P. U., Selsing J., Watson D., 2020, *ApJ*, 896, L20
- Johnson B. D., Leja J., Conroy C., Speagle J. S., 2021, *ApJS*, 254, 22
- Kalogera V. et al., 2021, The Next Generation Global Gravitational Wave Observatory: The Science Book, preprint ([arXiv:2111.06990](https://arxiv.org/abs/2111.06990))
- Kass R. E., Rafferty A. E., 1995, *J. Am. Stat. Assoc.*, 90, 773
- Kienlin von A. et al., 2020, *ApJ*, 893, 46
- Kilpatrick C. D., Malesani D. B., Fong W., 2020, *GCN Circ.*, 29133, 1
- Kouveliotou C., Meegan C. A., Fishman G. J., Bhat N. P., Briggs M. S., Koshut T. M., Paciesas W. S., Pendleton G. N., 1993, *ApJ*, 413, L101
- Krimm H. A. et al., 2020, *GCN Circ.*, 29139, 1
- Leibler C. N., Berger E., 2010, *ApJ*, 725, 1202
- Leja J., Johnson B. D., Conroy C., van Dokkum P. G., Byler N., 2017, *ApJ*, 837, 170
- Levan A., Crowther P., de Grijs R., Langer N., Xu D., Yoon S. C., 2016, *Space Sci. Rev.*, 202, 33
- Li Y., Zhang B., Lü H.-J., 2016, *ApJS*, 227, 7
- MacFadyen A. I., Woosley S. E., 1999, *ApJ*, 524, 262
- Madau P., Ferguson H. C., Dickinson M. E., Giavalisco M., Steidel C. C., Fruchter A., 1996, *MNRAS*, 283, 1388
- Malesani D. B., Knudstrup E., 2020, *GCN Circ.*, 29117, 1
- Mazets E. P. et al., 1981, *Ap&SS*, 80, 3
- Meegan C. et al., 2009, *ApJ*, 702, 791
- Minaev P. Y., Pozanenko A. S., 2020, *MNRAS*, 492, 1919
- Nakar E., 2007, *Phys. Rep.*, 442, 166
- Nava L. et al., 2012, *MNRAS*, 421, 1256
- Nicuesa Guelbenzu A. et al., 2011, *A&A*, 531, L6
- Nicuesa Guelbenzu A. et al., 2012, *A&A*, 548, A101
- Norris J. P., 2002, *ApJ*, 579, 386
- Norris J. P., Marani G. F., Bonnell J. T., 2000, *ApJ*, 534, 248
- Ohno M. et al., 2008, *PASJ*, 60, S361
- Omar A., Kumar T. S., Krishna Reddy B., Pant J., Mahto M., 2019, preprint ([arXiv:1902.05857](https://arxiv.org/abs/1902.05857))
- Page K. L. et al., 2020, *GCN Circ.*, 29112, 1
- Qin Y.-P., Xie G.-Z., Xue S.-J., Liang E.-W., Zheng X.-T., Mei D.-C., 2000, *PASJ*, 52, 759
- Rastinejad J. C. et al., 2021, *ApJ*, 916, 89
- Rastinejad J., Paterson K., Kilpatrick C. D., Fong W., 2020, *GCN Circ.*, 29142, 1
- Rossi A. et al., 2021, *ApJ*, 932, 15
- Rossi A., CIBO Collaboration, 2021, *GCN Circ.*, 29311, 1
- Sathyaprakash B. et al., 2012, *Class. Quantum Gravity*, 29, 124013
- Scargle J. D., Norris J. P., Jackson B., Chiang J., 2013, *ApJ*, 764, 167
- Sharma S. et al., 2022, *PASP*, preprint ([arXiv:2207.07878](https://arxiv.org/abs/2207.07878))
- Speagle J. S., 2020, *MNRAS*, 493, 3132
- Thöne C. C. et al., 2011, *MNRAS*, 414, 479
- Troja E. et al., 2016, *ApJ*, 827, 102
- Ugarte De Postigo A. et al., 2006, *ApJ*, 648, L83
- Ugarte de Postigo A. et al., 2014, *A&A*, 563, A62
- Ugarte de Postigo A., Kann D. A., Izzo L., Thoene C. C., Blazek M., Agui Fernandez J. F., Lombardi G., 2020, *GCN Circ.*, 29132, 1
- Ukwatta T. N. et al., 2010, *ApJ*, 711, 1073
- Valenti S. et al., 2017, *ApJ*, 848, L24
- Vianello G. et al., 2015, preprint ([arXiv:1507.08343](https://arxiv.org/abs/1507.08343))
- Woosley S. E., 1993, *ApJ*, 405, 273
- Woosley S. E., Bloom J. S., 2006, *ARA&A*, 44, 507
- Yonetoku D., Murakami T., Nakamura T., Yamazaki R., Inoue A. K., Ioka K., 2004, *ApJ*, 609, 935
- Yu Y. B., Li L. B., Li B., Geng J. J., Huang Y. F., 2018, preprint ([arXiv:1803.10040](https://arxiv.org/abs/1803.10040))
- Zhang B. B. et al., 2021, *Nature Astron.*, 5, 911
- Zhang B., 2006, *Nature*, 444, 1010

This paper has been typeset from a $\text{\TeX}/\text{\LaTeX}$ file prepared by the author.